INTERNATIONAL JOURNAL FOR NUMERICAL METHODS IN FLUIDS
Int. J. Numer. Meth. Fluids 2006; **51**:261–283
Published online 15 November 2005 in Wiley InterScience (www.interscience.wiley.com). DOI: 10.1002/fld.1120

Turbulence modelling of problem aerospace flows

Paul G. Tucker*,†

Civil and Computational Engineering Centre, School of Engineering, University of Wales, Swansea, Singleton Park, Swansea SA2 8PP, U.K.

SUMMARY

Unsteady Reynolds averaged Navier–Stokes (URANS) and detached eddy simulation (DES) related approaches are considered for high angle of attack NACA0012 airfoil, wing–flap, generic tilt-rotor airfoil and double-delta geometry flows. These are all found to be problem flows for URANS models. For DES fifth-order upwinding is found too dissipative and the use of, for high speed flows, instability prone centred differencing essential. An existing hybrid ILES–RANS modelling approach, intended for flexible geometry, relatively high numerical dissipation codes is tested along with differential wall distance algorithms. The former gives promising results. The standard turbulence modelling approaches are found to give perhaps a surprising results variation. Results suggest that for the problem flows, the explicit algebraic stress and Menter shear stress transport (SST) URANS models are more accurate than the economical Spalart–Allmaras (SA). However, the explicit algebraic stress model (EASM) in its k–ε form is impractically expensive to converge. Here, SA predictions lack a rotation correction term and this is likely to improve these results. Copyright © 2005 John Wiley & Sons, Ltd.

KEY WORDS: URANS; DES; ILES; aerospace; wall distance

1. INTRODUCTION

Especially in aerospace engineering, accurate turbulence modelling is a key design element. Perhaps, the most popular aerospace Reynolds averaged Navier–Stokes (RANS) model is that of Spalart and Allmaras [1]. This is referred to here as the Spalart–Allmaras (SA) model. For attached flows SA is generally both robust and accurate. Were it not for sensitivity to free stream turbulence conditions, the low Reynolds number k–ω model [2], which unlike the k–ε, more naturally links to the wall would be attractive. Observing the insensitivity of the k–ε model to free stream turbulence intensities Menter proposed the shear stress transport (SST) model [3]. Near walls this uses k–ω, a switching function giving k–ε modelling away

*Correspondence to: P. G. Tucker, Civil and Computational Engineering Centre, School of Engineering, University of Wales, Swansea, Singleton Park, Swansea SA2 8PP, U.K.
†E-mail: p.g.tucker@swansea.ac.uk

Contract/grant sponsor: U.K. Royal Academy of Engineering and Boeing

 Received 5 May 2004

from them. Unlike Reynolds stress models (RSMs) both SA and Menter SST cannot model turbulence anisotropy. For complex strain fields this is important. RSM predictions have been used to model airfoil flows (see Reference [4]). However, for routine industrial design calculations they are computationally expensive. The explicit algebraic stress model (EASM) [5] is potentially a cheaper RSM alternative that can predict anisotropy levels.

For massively separated flows, large geometry dependent more coherent eddies occur. Then the above RANS models become unsuitable [6]. For these flows hybrid RANS-LES like approaches [6, 7] have shown promise. The most popular is called detached eddy simulation (DES). With DES [6] most of the boundary layer is URANS modelled, the remaining flow area treated using LES. In Reference [7] just the inner part of the logarithmic layer is URANS modelled. A range of hybrid RANS-LES methods are well discussed by Davidson and Dahlstrom [8]. Simple non-separated flows present the strongest challenge to hybrid RANS-LES type approaches [9]. Hence, here it is proposed to partly explore the performances of hybrid RANS-LES related approaches for cases where generally the large majority of the lift surfaces have attached flow. For hybrid approaches to be reliable/useful design tools it is important that they offer sensible performance in this hybrid RANS-LES challenging regime.

The industrial application of hybrid RANS-LES is increasing. However, the more robust general solvers through which it is applied frequently rely on lower (typically second or third) order (see, for example, References [10, 11]) *upwind* schemes. This is entirely understandable, since, to directly quote from Reference [12] 'most aerodynamic codes able to deal with complex geometry are based on the finite volume technique in order to handle degenerated cell. Thus getting a higher-order method becomes very time consuming because of the high-order quadrature needed to compute the fluxes along the cell boundaries'. More importantly, general purpose, robust solvers tend to rely on dissipative upwind type convective schemes. For stability and hence robustness reasons these are attractive. However, the stability comes through the introduction of excessive numerical dissipation (excessive numerical dissipation can also arise due to preconditioning issues). For convective term discretization, to improve accuracy, LES type simulations have incorporated fifth-order upwind schemes. However, even then, for relatively simple geometries (see References [13, 14]) numerical dissipation can be so high that the subgrid scale model has little effect. When solutions are switched to third-order upwind (see References [13, 15]) serious errors can occur. In the work of, for example, Garnier *et al.* [15], when applying the third-order upwind version of Roe's [16] flux difference-splitting algorithm, subgrid scale model omission was recommended. To remedy this, blending (see References [17, 18]) of upwind and central difference schemes just in separation zones has been attempted (the upwind component is retained for stability reasons). However, although superior, such approaches again increase code complexity. Also, they can have an *ad hoc* nature regarding the level of blending, where the blending should occur and how gradually transition between nominally upwind and centred zones is affected. Understandably, industrial, complex geometry hybrid RANS-LES related applications tend to use grids that are coarser than desirable. Such simulations also tend to use stable lower order upwind differences. Then the monotone-integrated LES (MILES) approach (see Reference [19]) where the subgrid scale model is omitted and the dissipative numerical error used to drain turbulence becomes, in a pragmatic sense, sensible (see Reference [15]). However, near walls turbulence structures become excessively complex and fine for sensible numerical resolution. As noted by Boris *et al.* in this region the isotropy assumption of most LES subgrid scale models

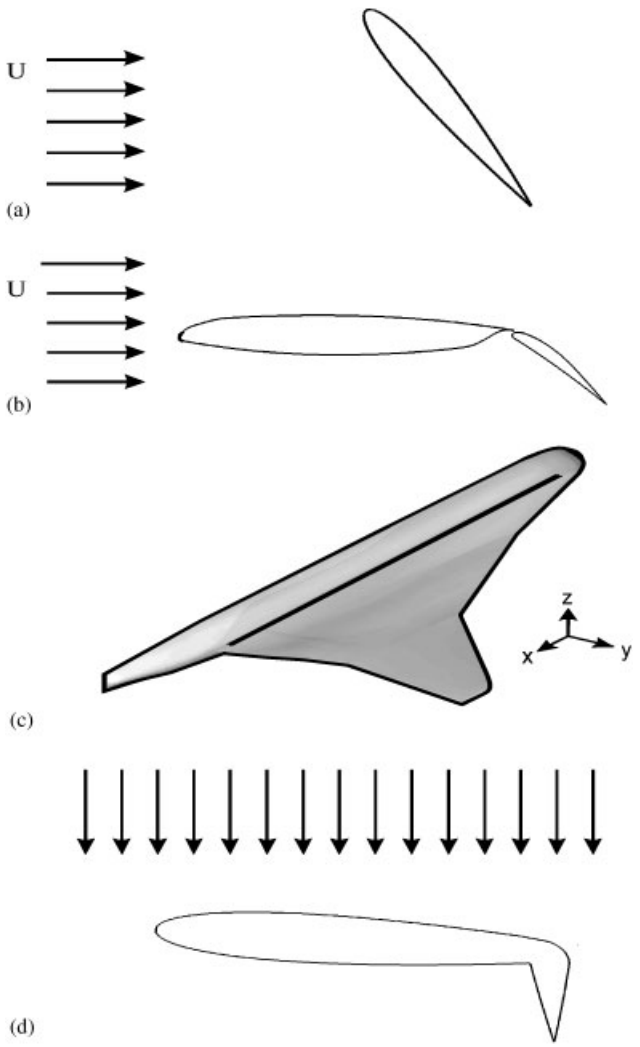

Figure 1. Geometries considered: (a) NACA0012; (b) wing–flap; (c) double-delta; and (d) generic tilt-rotor wing.

becomes invalid. Further more, as indicated by Fureby and Grinstein [20], near wall grids can become highly anisotropic thus erroneously resolving isotropic components differently in different co-ordinate directions. Severe near wall grid stretching also introduces filter commutation errors. Thus near wall LES modelling becomes unattractive. However, in this region MILES also has disadvantages. One being that, unlike LES, the implied subgrid scale stress cannot, as it should, vanish. Therefore, for the above reasons, it would seem helpful to retain a computationally economical RANS model in this near wall region. These industrial design related modelling considerations suggest the hybrid approach of Tucker [21] where MILES (or implicit LES–ILES—acknowledeging that not just monotone schemes can be used to re-

place the subgrid scale model) is used away from walls and RANS near them. However, this would leave a solution with a discontinuous 'turbulence length scale', the RANS scale growing with wall distance (d) and then suddenly dropping to zero at the MILES/ILES zone. This can be overcome by blending through use of a Laplacian. Tucker [21, 22], for example solves the Eikonal wall distance [23] equation by marching it to the ILES–RANS interface, a Laplacian being then added to blend the very different RANS and ILES length scales. The same hybrid ILES–RANS approach is tested here and contrasted with pure ILES. Also, the SA DES technique [6] is tried with different C_{DES} (equivalent to the Smagorinsky constant but in an SA LES framework) values along with the Menter SST based DES of Strelets [18]. The following URANS models are also considered: SA, Menter SST and the EASM of Gatski and Speziale [5] in a k–ε framework. It is worth noting that hybrid ILES–RANS is, under certain circumstances, possibly a limiting case of standard SA DES. If C_{DES} and numerical accuracy are sufficiently low, away from walls numerical dissipation could dominate but the near wall RANS modelling still be active.

The following Figure 1 geometries are considered: (a) NACA0012 at a 60° angle of attack; (b) a wing–flap configuration; (c) a double-delta wing configuration and an (d) idealized tilt-rotor airfoil geometry. Case (b) exhibits separation over part of the flap. The frame (c) (Case (c)) flow has leading edge separation. Cases (a) and (d) are used more as an extreme, illustrating hybrid scheme performances/traits for highly separated flows, the other cases involving relatively little separation.

2. NUMERICAL MODELLING

2.1. Equations of motion

Conservation of momentum is expressed using Equation (1) below:

$$\frac{\partial \rho \tilde{u}_i}{\partial t} + \frac{\partial \rho \tilde{u}_i \tilde{u}_j}{\partial x_j} = -\frac{\partial \tilde{p}}{\partial x_i} + \frac{\partial \tilde{\tau}_{ij}}{\partial x_j} \tag{1}$$

The symbol $\tilde{u}_i$ is a fluid velocity component, ρ density, μ viscosity (evaluated from Sutherland's equation), $\tilde{p}$ static pressure, t time and x the spatial co-ordinate. The stress tensor, $\tilde{\tau}_{ij}$, in Equation (1) is calculated using

$$\tilde{\tau}_{ij} = 2(\mu + \mu_T)\left[\tilde{S}_{ij} - \frac{1}{3}\frac{\partial \tilde{u}_j}{\partial x_j}\delta_{ij}\right] \tag{2}$$

where δ_{ij} is the Kronecker delta ($\delta_{ij} = 1$ if $i = j$ and $\delta_{ij} = 0$ if $i \neq j$). The strain rate tensor, $\tilde{S}_{ij}$, is expressed as

$$\tilde{S}_{ij} = \frac{1}{2}\left(\frac{\partial \tilde{u}_i}{\partial x_j} + \frac{\partial \tilde{u}_j}{\partial x_i}\right) \tag{3}$$

The tilde and T subscript in the above equations are used to highlight or help identify that in this work the variables can have dual meanings. For example, with pure URANS simulations temporal phase averaged variables are resolved. On the other hand, with the hybrid simulations

away from walls variables are spatially averaged. Consequently, in URANS simulations or regions $\mu_T = \mu_t$, the eddy viscosity. For LES zones $\mu_T = \mu_{\text{sgs}}$, the subgrid scale viscosity. For ILES $\mu_{\text{sgs}} = 0$, i.e. effectively $\mu_T = \mu_{\text{num}}$ the numerical diffusion. In conjunction with the above, for compressible flow, the following conservation of energy equation is solved

$$\frac{\partial \tilde{E}}{\partial t} + \frac{\partial}{\partial x_j}(\tilde{u}_j(\tilde{E} + \tilde{p})) = \frac{\partial}{\partial x_j}(\tilde{u}_i \tilde{\tau}_{ij}) - \frac{\partial \tilde{q}_j}{\partial x_j} + \frac{\partial \tilde{\psi}_j}{\partial x_j} \tag{4}$$

For the linear URANS and hybrid models $\tilde{\psi}_j = 0$. The total energy (internal and kinetic) per unit volume is expressed as

$$\tilde{E} = \rho e + \tfrac{1}{2}\rho \tilde{u}_i \tilde{u}_i \tag{5}$$

where $e = C_v T$ and C_v is the constant volume specific heat. Note that in Equation (5) the turbulent kinetic energy (k) contribution to $\tilde{E}_i$ is ignored, i.e. $k \ll \rho e + \frac{1}{2}\rho \tilde{u}_i \tilde{u}_i$. Pressure, temperature (T) and ρ are related through the equation of state for a perfect gas $\tilde{p} = \rho R \tilde{T}$. For the heat flux q_j the following is used:

$$\tilde{q} = -(\hat{k} + \hat{k}_T)\frac{\partial \tilde{T}}{\partial x_j} \tag{6}$$

In the above, $\hat{k}$ is the thermal conductivity. Also, $\hat{k}_T = C_P \mu_T / Pr_T$ where C_p is the specific heat at constant pressure and $Pr_T = 0.9$ is the turbulent Prandtl number. It follows that in the ILES zone since $\mu_T = 0$, $\hat{k}_T = 0$. The continuity equation to go with the above is

$$\frac{\partial \rho}{\partial t} + \frac{\partial \rho \tilde{u}_j}{\partial x_j} = 0 \tag{7}$$

2.2. Turbulence models

Most of the turbulence models used are established and well detailed in references given in the introduction. Therefore, generally, only brief descriptions of these are given. The less standard or well-known models are perhaps the DES, hybrid ILES–RANS and EASM. Hence, for these, more details are given. However, first URANS models are outlined and then their DES/LES/ILES extension. As noted, in URANS mode, the following models are used (a) SA; (b) Menter SST and (c) EASM. Due to the flow separation, only in the URANS mode full convergence can be gained (unless of course the base discretization is too dissipative).

SA solves a single eddy viscosity convection/diffusion transport equation. Menter SST is in a sense hybrid, solving the k–ω model near walls and the k–ε away from them. It merges the differing k–ω/k–ε models through a weighting expression having a similar form to Equation (17) shown later. The Menter SST k transport equation has the length scale $l_{k-\omega}$.

The EASM (model (c)) is solved in a k–ε framework. With it, Equation (2) extends to

$$\tilde{\tau}_{ij} = 2\mu_T \left[\tilde{S}_{ij} - \frac{1}{3}\frac{\partial \tilde{u}_j}{\partial x_j}\delta_{ij}\right] - \frac{2}{3}\rho \tilde{k}\delta_{ij} + 2\mu_T C_1 \frac{k}{\varepsilon}\left[\tilde{S}_{ik}W_{kj} - W_{ik}\tilde{S}_{kj}\right]$$

$$-2\mu_T C_2 \frac{k}{\varepsilon}\left[\tilde{S}_{ik}\tilde{S}_{kj} - \frac{1}{3}\tilde{S}_{kl}\tilde{S}_{lk}\delta_{ij}\right] \tag{8}$$

where C_1 and C_2 are standard constants. Also

$$W_{ij} = \frac{1}{2}\left(\frac{\partial \tilde{u}_i}{\partial x_j} - \frac{\partial \tilde{u}_j}{\partial x_i}\right) \tag{9}$$

and

$$\tilde{\psi}_j = \left(\mu + \frac{\mu_T}{\sigma_k}\right)\frac{\partial k}{\partial x_j} \tag{10}$$

where σ_k the Schmidt number for k.

It is straightforward to convert most of the above into 'zonal LES' models. For SA based DES the RANS model d is replaced by

$$\tilde{d} = \min(d, C_{\mathrm{DES}}\Delta_i) \tag{11}$$

As proposed by Rollet-Miet *et al.* [9], using for convenience in a Cartesian coordinate system

$$\Delta_i = \max(\Delta x, \Delta y, \Delta z) \tag{12}$$

However, other definitions are possible, for example, the following volume based expression:

$$\Delta_i = (\Delta x \Delta y \Delta z)^{1/3} \tag{13}$$

For SA DES, where $C_{\mathrm{DES}}\Delta_i < d$ essentially a Smagorinsky LES model is gained. For Menter SST based DES (see Reference [18]) the k equation $l_{k-\omega}$ is replaced by

$$\tilde{l}_{k-\omega} = \min(l_{k-\omega}, C_{\mathrm{DES}}\Delta_i) \tag{14}$$

2.3. Wall distances and hybrid ILES–RANS

In all of the above models, essentially the near wall turbulence length scale $l = f(d)$. When using search procedures d is surprisingly expensive to compute [24, 25]. It can potentially be more economically evaluated from the following equation (see Reference [21]):

$$n|\nabla\phi| = 1 + f(\phi)\nabla^2\phi + g(\phi) \tag{15}$$

using one of two approaches. For the indirect approximate approach (i) (see Reference [26]), $n = g(\phi) = 0$, $f(\phi) = 1$ in Equation (15) and

$$d = \pm\sqrt{\sum_{j=1,3}\left(\frac{\partial\phi}{\partial x_j}\right)^2} + \sqrt{\sum_{j=1,3}\left(\frac{\partial\phi}{\partial x_j}\right)^2 + 2\phi} \tag{16}$$

Equation (16) is derived by making a one-dimensional Poisson equation analytical solution. With approach (ii) $n = 1$, $f(\phi) = \varepsilon_0\phi$, $g(\phi) = \varepsilon_1(\phi^e/L)^m$ and $d = \phi$, or in a DES context (see later) $\tilde{d} = \phi$. The length scale L is the RANS region width (see Figure 2) and m is a positive integer. When $\varepsilon_0 = \varepsilon_1 = 0$, Equation (15) reduces to the exact wall distance, hyperbolic natured, Eikonal equation. The Eikonal equation can be solved by propagating fronts from solid surfaces [23]. With the starting condition $d = C_{\mathrm{DES}}\Delta_i$ the front propagation naturally stops at the RANS/LES interface of a DES solution. The computed distance field can then be imported into a standard CFD program with the SA URANS model activated and an SA

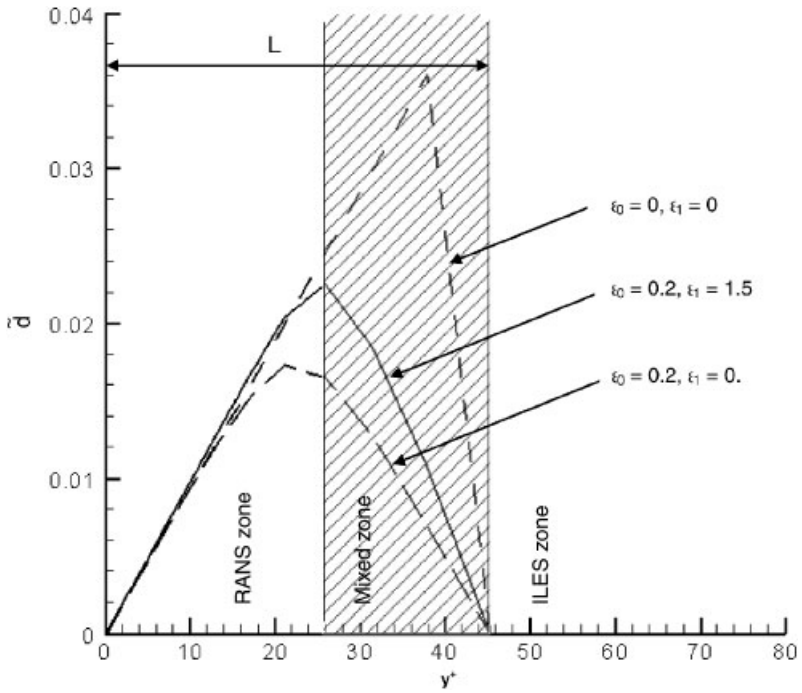

Figure 2. Hybrid ILES–RANS turbulence length/distance scales.

DES solution will automatically result. No core solver changes are required. With ε_0, $\varepsilon_1 > 0$ Equation (15) is a Hamilton–Jacobi equation. For hybrid ILES–RANS the Eikonal equation can propagated towards the RANS/ILES interface. Then, inside the ILES region $d = 0$ (or in this context $\tilde{d} = 0$). Finally, the Hamilton–Jacobi equation is solved. The Laplacian in this enables a smooth $\tilde{d}$ transition between the RANS and ILES zones. The function $g(\tilde{d})$ can be used to control the abruptness of the RANS length scale change as the ILES region is approached. The Hamilton–Jacobi equation $\tilde{d}$ field can again be imported into a standard URANS CFD solver (with a wall distance based turbulence model activated) and a hybrid ILES–RANS solution will arise.

Figure 2, shows potential Equation (15) hybrid ILES–RANS $\tilde{d}$ length scales (the ILES–RANS interface is set at, in the context for the current work, the arbitrary value of $y^+ \approx 45$). The full line is for $\varepsilon_0 = 0.2$ and $\varepsilon_1 = 1.5$. The long dashed is for $\varepsilon_0 = 0.2$, $\varepsilon_1 = 0$ and $m = 1$. The short dashed line is the pure Eikonal solution ($\varepsilon_0 = \varepsilon_1 = 0$) stopped at the RANS/ILES interface. Here ILES–RANS interfaces correspond to where they would occur for standard SA DES (with SA used for the RANS model). Hence L can vary with surface location. Since, for complex grid structures the DES L value can be discontinuous (see later) this is perhaps not a good practice. Here, as a partial remedy for the complex grid structures, where $|\nabla L| \to \infty$, both L and $\tilde{d}$ are Laplacian smoothed as described in Reference [22] (i.e. the Laplacian is not applied through the Hamilton–Jacobi equation but as a separate operation on a d field). For SA and EASM solutions either (16) or the Eikonal equation used for d. Other solutions

generally use a search procedure. However, it has been verified [26] that the current URANS results are insensitive to the d evaluation strategy.

2.4. Solution of flow equations

The aerospace flow cases are solved using structured grid finite volume approaches having second-order backwards difference temporal discretizations. All DES/ILES/LES type simulations use Courant numbers of less the unity. Typically they are much smaller than this. For the aerospace cases convective fluxes are discretized using Roe's [16] flux difference splitting scheme. Essentially, these fluxes can be considered as

$$J_{\text{conv}} = (1 - \alpha)J_{\text{ctr}} + \alpha J_{\text{upw}} \tag{17}$$

where J_{ctr} and J_{upw} are central and upwind difference components and α is a weighting parameter. The parameters N_{CD} and N_{UP} define the order of central difference and upwind solution components, respectively. For diffusion terms second-order central differences are used. For the aerospace flows, the Navier–Stokes equations are discretized in their strong conservation form. For the less separated flow Cases (b) and (c) cross-terms are neglected in the discretized equations. For all cases, average first off wall grid nodes are at $y^+ < 1$. Cases (a) and (b) use periodic cross-stream boundary conditions. The wing–flap and double-delta geometry cases are run in MPI parallel processing mode. Note, Cases (a) and (d) use a modified version of the NTS solver described in References [6, 8]. Cases (b) and (c) use a modified version of the NASA CFL3D solver.

3. RESULTS AND DISCUSSION

With the exception of Case (d), test cases are presented in order of decreasing separation. Hence, broadly speaking, the initial cases are, theoretically, more URANS challenging. Conversely the latter are more hybrid RANS-LES/ILES challenging, the exception being Case (d). Hybrid ILES–RANS validation cases for an $Re_\tau \approx 1000$ plane channel flow using SA RANS are discussed in Appendix A. For all Figure 2 ε_0, ε_1 combinations tested the 'law of the walls' are found to be reasonable.

3.1. NACA0012 (Case (a))

The set-up for this 60° angle of attack case is as in Reference [6]. Therefore, only brief details are given here. The 'O' grid has 142 radial nodes, 61 nodes wrapped around the wing surface and 26 nodes in the cross-stream direction. The cross-stream domain width is equal to the wing chord. For $Re = 1 \times 10^5$ (based on the chord) the measured lift (C_{L}) and drag (C_{D}) coefficients are about 0.925 and 1.65, respectively. Hybrid ILES–RANS results are found insensitive to Figure 2 ε_0, ε_1 combinations. Table I gives C_{L} and C_{D} values for various solution approaches. Negative signs are used to represent magnitude under-predictions. The first table entry shows the large error values for the Menter SST URANS model. As will be seen later, this model is perhaps the best of all the URANS models considered here. The poor Menter SST performance is because URANS models have insufficient solution physics

Table I. Summary of Case (a) C_L and C_D errors.

Model	Discretization	Errors	
		$\%C_L$	$\%C_D$
Menter SST (URANS)	$\alpha = 1$, $N_{UP} = 5$	72	64
SA DES	$\alpha = 1$, $N_{UP} = 5$	19	13
SA DES	$\alpha = 0.1$, $N_{UP} = 5$, $N_{CD} = 4$	9	3
Menter SST DES	$\alpha = 1$, $N_{UP} = 5$	12	5
ILES	$\alpha = 1$, $N_{UP} = 3$	12	4
Hybrid ILES–RANS	$\alpha = 1$, $N_{UP} = 3$	12	4
Hybrid ILES–RANS*	$\alpha = 1$, $N_{UP} = 3$	−1	−9

embodied in their modelling to account for the highly geometry dependent eddies arising from massively separated flows [6].

Comparison of the second and third table entries shows that for DES, where there is a subgrid scale model to dissipate turbulence, centred differencing is very important. The blended central differencing is just applied in the separated wake region using the method of Strelets [18]. For solutions with a ILES component, to assist turbulence dissipation $\alpha = 1$ and $N_{UP} = 3$. As might perhaps be expected for this massively separated, negligible boundary layer content flow, the ILES performance is reasonable. In fact, relative to SA DES, the potentially greater level of resolved turbulence activity has given improved accuracy.

For this high angle of attack case there is relatively little boundary layer shear and hence modelled turbulence generation. Also, with the hybrid ILES–RANS the modelled turbulence away from solid surfaces is zero. Furthermore, the free-stream flow convects this zero modelled turbulence level into the near wall region. The combination of these factors results in laminarization of the modelled hybrid ILES–RANS turbulence component. Hence, the ILES and hybrid ILES–RANS results are virtually the same. However, with the satisfactory ILES performance this is of no great concern. For the hybrid ILES–RANS* solution, shown in the last table entry, the SA DES near wall modelled component is frozen and used in a 'hybrid ILES–RANS' solution. This has resulted in an extremely accurate C_L prediction but C_D has deteriorated. Even so, both these values are better than those for standard SA DES with $N_{UP} = 5$. The significant levels of resolved flow activity, which is enhanced by ILES use can be seen in Figure 3 hybrid ILES–RANS* vorticity plot.

Of course, the more challenging regime for the hybrid eddy resolving-RANS approaches is where there is minimal separation. For an angle of attack of 5° (i.e. a low angle away from the hysteresis zone in C_L, C_D against angle of attack plots) the C_L errors for the hybrid ILES–RANS, SA DES and ILES are 4.94, −10.73 and −21.39%, respectively. It is difficult to explain why the hybrid ILES–RANS has better accuracy than SA DES. The hybrid ILES–RANS also has the best C_D accuracy with again ILES being worst.

3.2. *Wing–flap flow* (*Case* (*b*))

For Case (b) the wing and flap angles are 2 and 40°, respectively. The gap between the wing and flap is 0.6% of the wing chord. The Reynolds number is 23×10^6 (based on chord) and the Mach number 0.18. Flow simulations use $\alpha = 1$ and $N_{UP} = 3$. The measured C_L is 2.27.

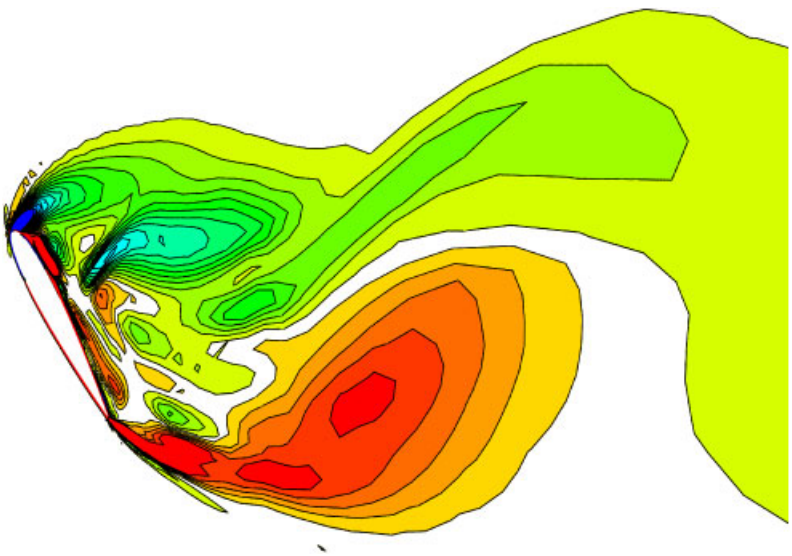

Figure 3. Hybrid ILES–RANS* instantaneous vorticity plot for NACA0012.

Figure 4 gives $x-y$ plane views of the wing–flap local grid, along with SA DES turbulence 'length scales' and wall local Eikonal distances. For hybrid ILES–RANS a Laplacian blends such distances [22] with the ILES zone. The $x-y$ plane uses just under 0.1 million grid points. This is sufficient for RANS solution grid independence. The vertical domain is chosen to exactly match the wind tunnel extent, the solid walls of which are treated using no-slip boundary conditions. For DES, ILES and hybrid ILES–RANS simulations a periodic cross-stream domain is used with 33 grid nodes and an extent of 2.5 times the flap length. The Figure 4(b) turbulence length scale is based on Equation (13). This usefully illustrates the SA DES problem that $\tilde{d}$ can, for more complex grid systems, become non-smooth. For the present case, with Equation (12) this non-smoothness is remedied. However, for the three-dimensional double-delta geometry it is evident even with a $\Delta_i = \max(\Delta x \Delta y \Delta z)$ 'filter'.

Unfortunately, the measurements compared with here are made in the identical small working section wind tunnel, with a similar high-lift configuration to that considered by Rumsey *et al.* [27]. Numerical comparisons for the latter suggest excessive wind tunnel wall and mounting bracket influence. Therefore, the current computations are perhaps, in part, best considered as suggestive of potential solution sensitivities with respect to turbulence modelling for high-lift configurations.

Figure 5 compares pressure coefficient (C_p) predictions with measurements. There is a significant difference between the SA RANS (dash–dot line), Menter SST (dashed line) and EASM (full line) results. The hybrid ILES–RANS is shown using a dotted line. As noted by Strelets [18], the choice of underlying RANS model in a DES simulation alters the separation point location. Hence it has a strong solution influence. Since, there is a significant difference between SA and Menter SST URANS, both these models are compared in a DES context along with ILES and hybrid ILES–RANS simulations. Table II summarizes predicted C_L errors

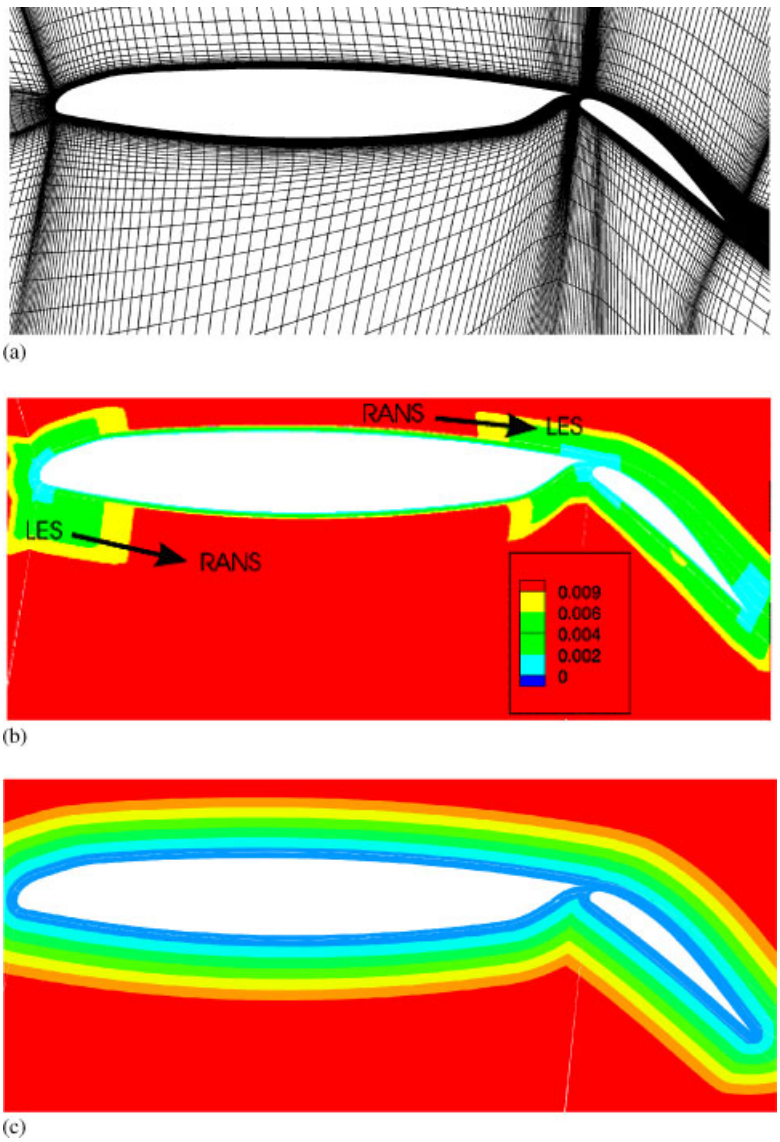

Figure 4. Grid and turbulence 'length scales:' (a) grid; (b) DES 'length scale' (2D); and (c) Eikonal d (near wall).

for the different models. A negative sign indicates a lift under prediction. Table entries are ordered with decreasing predicted C_L. SA gives the worst C_L over-prediction and ILES the biggest under-prediction. For the URANS predictions, changing to three-dimensional solutions generally only has a minor accuracy benefit. Relative to SA URANS, SA DES improves agreement with measurements. Also, reducing C_{DES} to 0.1, to partly give a more hybrid ILES–RANS like solution (i.e. less dissipation in the wake region) produces a further agreement with

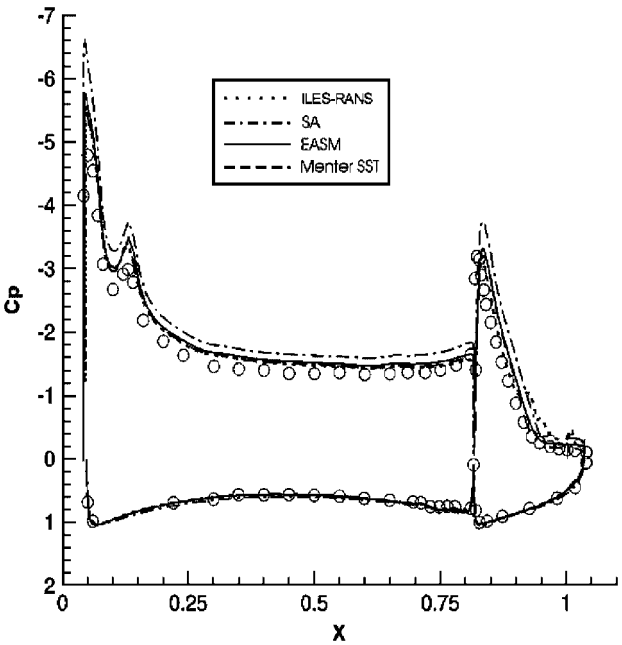

Figure 5. Comparison of C_p measurements with predictions.

Table II. Summary of Case (b) (wing–flap configuration) C_L errors.

Model	$\%C_L$ 'Error'
SA URANS	16
SA DES	10
EASM URANS	7
Menter SST URANS	7
SA DES ($C_{DES} = 0.1$)	2
Menter SST DES	−3
Hybrid ILES–RANS	−5
ILES	−16

the measurements. Both the EASM and Menter SST URANS models have lower deviations from the measured C_L than SA. The improved C_L agreement for Menter SST DES relative to SA DES reflects the ability of the Menter SST URANS model to capture the flap separation point.

Figure 6 gives flap region helicity contours for the 3D Menter SST URANS and DES, and hybrid ILES–RANS simulations. The contours suggest the URANS solution is quasi two dimensional and that, as would be expected, the hybrid ILES–RANS has strongest resolved activity. Figure 7 gives vorticity contours for the Menter SST DES (Frame (a)), hybrid ILES–RANS (Frame (b)) and ILES (Frame (c)). Again, as might be expected, the wake region extent increases with ILES solution content. Perhaps, surprisingly for the pure ILES solution

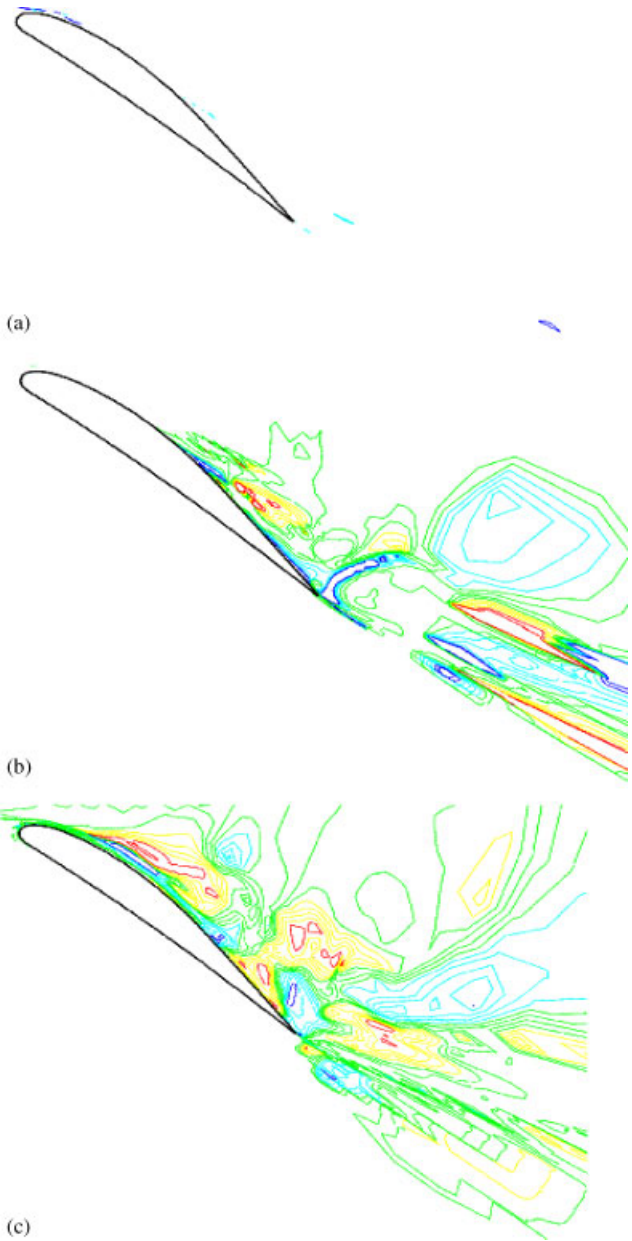

Figure 6. Wing–flap helicity contours: (a) Menter SST URANS; (b) Menter SST DES; and (c) hybrid ILES–RANS.

the boundary layer flow adjacent to the top airfoil surface appears to have large unsteady structures. The hybrid ILES–RANS flow field appears more physically plausible. Also, its C_L value is second closest to the measured value.

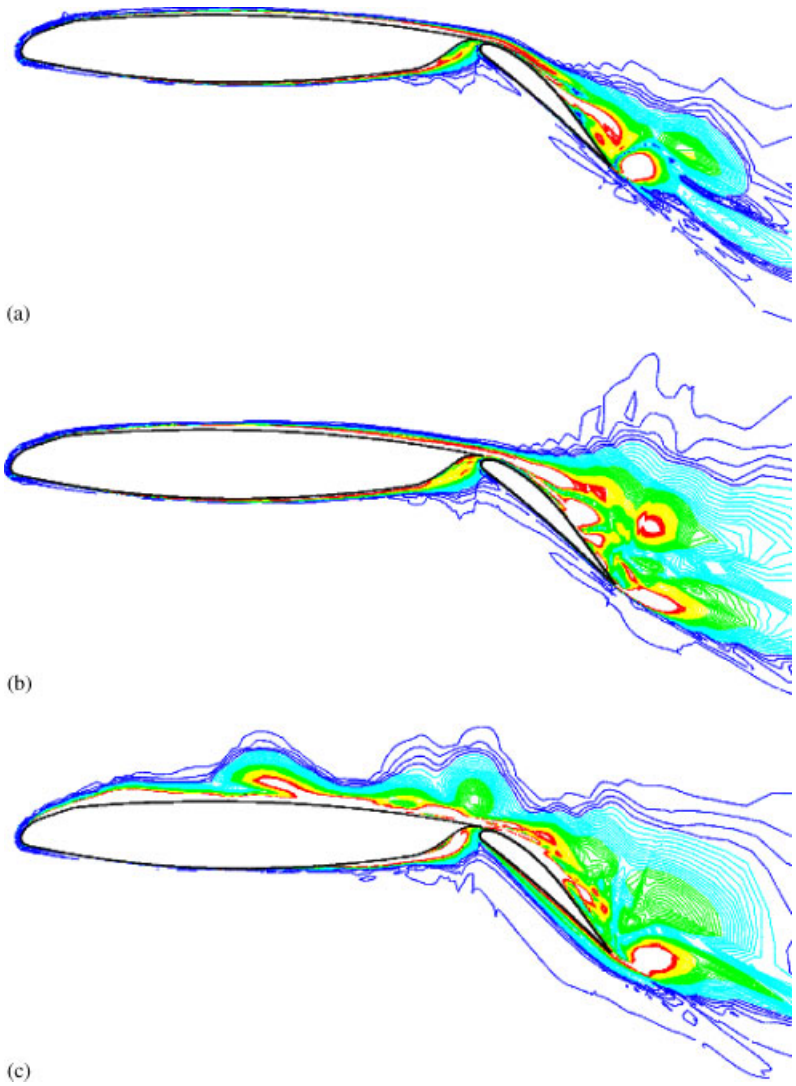

Figure 7. Wing–flap configuration vorticity contours: (a) Menter SST based DES; (b) hybrid ILES–RANS; and (c) ILES.

3.3. *Double-delta wing configuration* (*Case* (*c*))

For this $Re = 2.2 \times 10^6$ (based on half wing span) case the Mach number is 0.96. The angle of attack is low at 6°. Also, a 28 block grid, having 1.2×10^6 cells is used with $\alpha = 1$ and $N_{\mathrm{UP}} = 3$. Figure 8 presents some Case (d) turbulence length scale related information. Frame (a) gives SA DES contours of distance, in wall units, for the RANS/LES interface location, i.e. L^+. Frame (b) gives the surface grid and distance contours from Equation (15) with

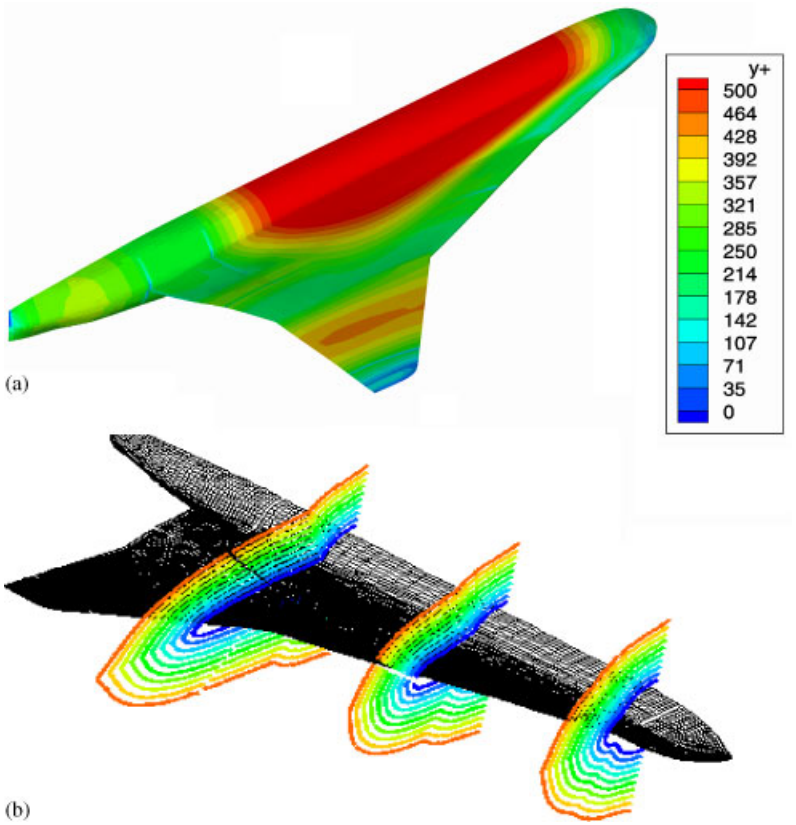

Figure 8. Double-delta wing distance related parameters: (a) d^+ contours of LES–RANS interface for SA DES with $C_{DES} = 0.025$; and (b) distance contours from Equation (15) in Eikonal form (Note, distances shown are well beyond those needed for hybrid applications).

$\varepsilon_0 = \varepsilon_1 = 0$. For hybrid ILES–RANS solutions just near surface distances are used. The Frame (b) surface grid illustrates the significant non-uniform grid spacing variations around the grid block interfaces. As Figure 8(a) suggests, reminiscent of Figure 4(b), these non-uniform regions give rise to significant variations in the SA turbulence length scale distribution and a ragged RANS/LES interface. This non-uniformity is because the location is grid controlled. Work attempting to address this problem, through interface region specification is discussed by Tucker and Davidson [7] and Temmerman *et al.* [28]. Another point to note from Figure 8 is that, although a very low C_{DES} value of 0.025 is used, in some places L^+ is large. In fact, with the standard C_{DES} value of 0.65, in certain places $L^+ \approx 13\,000$. Conversely, the fine wing tip grid results in an interface location that tends to be around the inner part of the logarithmic layer.

Figure 9 compares Case (c) RANS, DES and hybrid ILES–RANS C_p predictions with measurements. The triangle and circle symbols give the wing upper and lower surface C_p measurements, respectively. The lines give the various predictions. Pressure coefficient comparisons are made at the four Figure 10 locations. These are at $10, 30, 60$ and 95% of

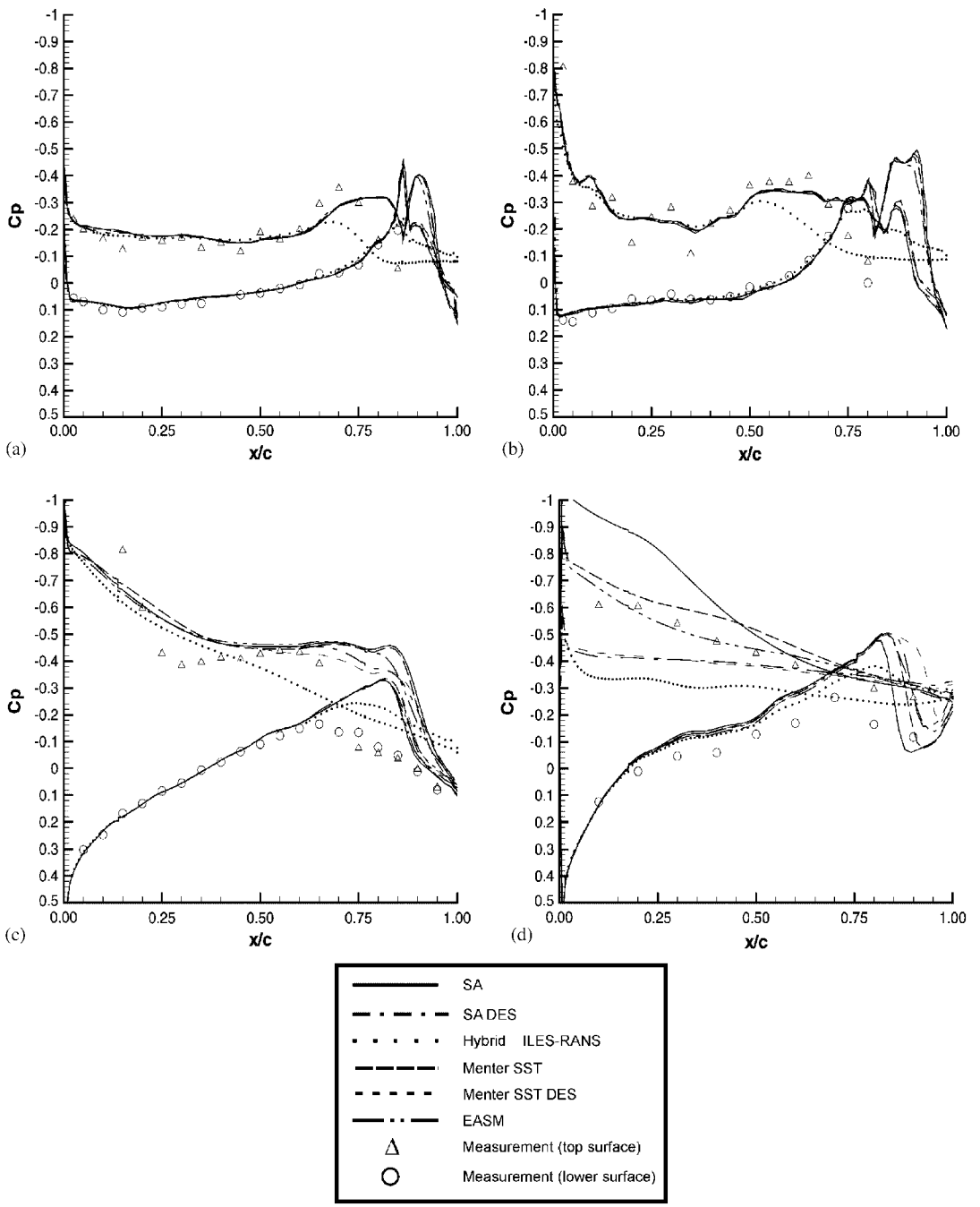

Figure 9. Comparison of double delta C_p measurements with predictions: (a) 10% across wing; (b) 30% across wing; (c) 60% across wing; and (d) 95% across wing.

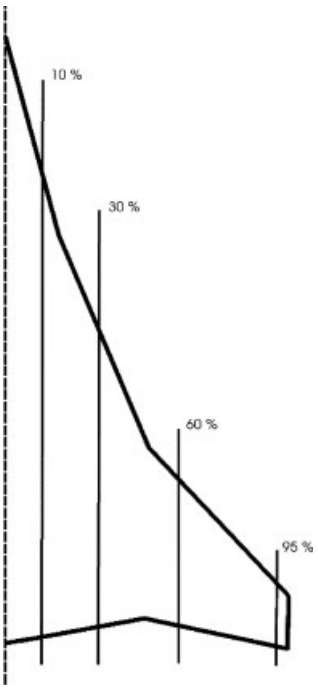

Figure 10. Locations of double delta C_p comparisons.

the wingspan. Despite the low angle of attack, the extent of the separated vortical region is significant. This suggests that the DES and the hybrid ILES–RANS methods might give some benefits. Figure 9(a) shows that for the attached flow inboard wing region all models give similar results. At 10 and 30%, the agreement with measurements seems reasonable. It could be argued the hybrid ILES–RANS results, given by the dotted line, show the best trends. However, at 60% and $x/c > 0.7$ predicted C_p values clearly deviate from the measurements. For example, at 60% the top surface measurements suggests the C_p distribution at $x/c \approx 0.75$ should have an inflexion. The hybrid ILES–RANS solution profile is closest to this state be clearly not inflexional. At 95% large differences in both trends and magnitudes are evident between the models. For example, the SA model suction pressures (full line) are too high. Conversely the hybrid ILES–RANS are too low. The short then long dashed line represents the SA DES. The integrated error for this (see later) is less than for SA but the solution shows little unsteadiness. Conversely, as shown in Figure 11, the hybrid ILES–RANS gives strong unsteadiness in the outboard region with vortex structures propagating over the upper wing surface. These vortex structures and the added modelling challenge that they introduce might explain the deviations between predictions for the larger x/c values. Alternatively, they might be a consequence of having too little near wall modelling (cf. Figure 7(c)) i.e. too small an L^+. This aspect will be discussed further later. As can be seen from Figure 9, the Menter SST (the long dashed line) gives better predictions than SA, but in DES mode the results for these models are quite similar. Overall the EASM (long dashed and two short dashes) shows better agreement than the Menter SST.

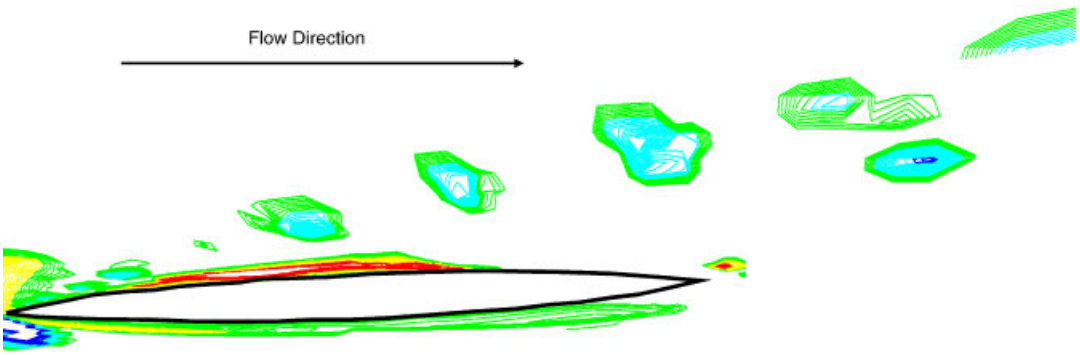

Figure 11. Hybrid ILES–RANS near wing tip helicity contours for double-delta configuration.

Table III. Summary of Case (c) PEP errors.

Model	PEP
SA	2.6
SA DES	2.5
Menter SST	2.4
Menter SST DES	2.5
EASM	2.3
Hybrid ILES–RANS	2.2

In the absence of C_L data, to make more quantitative comparisons the following pressure error parameter (PEP) is defined:

$$\mathrm{PEP} = \sum_{1-4} \left(\sum_{i=1,\mathrm{np}} |C_{\mathrm{p,num}} - C_{\mathrm{p,exp}}| \Delta s_i \right) \tag{18}$$

where np is the number of experimental data points on each of the four profiles. Also, $C_{\mathrm{p,num}}$ and $C_{\mathrm{p,exp}}$ are the predicted and measured lift coefficient values. The parameter, Δs_i is the surface length over which the pressure can be considered to act (a piecewise linear pressure distribution is effectively assumed). Table III gives PEP values for the different models. The larger PEP the greater the error.

Results suggest, as in the work of Morton *et al.* [29], that SA is too dissipative to model the vortical flows characteristic of delta wings. RANS solutions with the SA-rotation correction (see Morton *et al.* [29]) might well improve predictions. Table III shows the EASM is the most accurate Case (c) URANS model. However, it proved very expensive to converge. Considering that this is a non-ideal DES type method case, the hybrid ILES–RANS model results show promise. However, observation of the Figure 9 hybrid ILES–RANS C_p curves suggest the PEP value for this approach might be slightly flattering, i.e. at 95% across the wing the hybrid ILES–RANS top surface C_p distribution is worst of all the models. Since the wing tip surface area is relatively small the PEP is not greatly influenced by these C_p values.

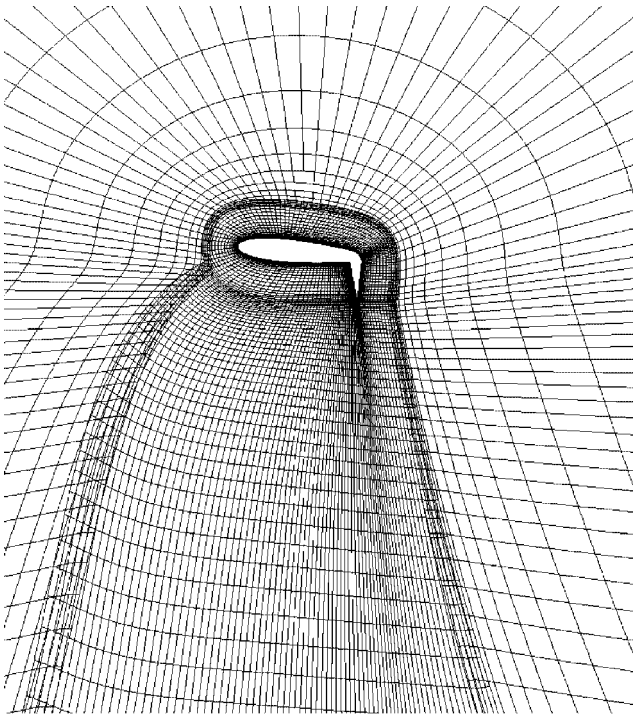

Figure 12. Tilt-rotor wing grid.

The Case (c) hybrid ILES–RANS length scale approximates to the $\varepsilon_0 = 0.2$, $\varepsilon_1 = 1.5$ profile in Figure 2. However, the SA DES profile is more akin to that for $\varepsilon_0 = \varepsilon_1 = 0$ (but without the abrupt length scale drop). Hence, for SA DES the integrated near wall modelled component is greater. Also, as implied earlier, the grid is such that at the wing tip L tends to be small. The diminished hybrid ILES–RANS integrated modelled length scale combined with the already small L makes the wing tip modelling more akin to ILES than ILES–RANS. This probably explains why the ILES–RANS solution is not so good in this region. However, clearly with the hybrid ILES–RANS approach control of the level and spatial extent of the RANS modelling can be exerted through L, ε_0 and ε_1 (as noted earlier the Hamilton–Jacobi turbulence length scales have not been used for this case or the previous). It is therefore likely a hybrid ILES–RANS interface with a constant L value based on turbulence physics and not grid would give better results. This aspect is left as future work.

3.4. Tilt-rotor airfoil (Case (d))

There is no direct measurement data for this $Re = 3 \times 10^5$ case. The geometry is quite similar to that found in Reference [30] the case set-up and mesh topology (involving about 0.6 million cells) being identical. Hence only brief case details are given here. The key point of this final case is to further illustrate the importance of wall modelling even on cases with minor boundary layer content. Figure 12 shows a two-dimensional plane view of the multi-block mesh. Figure 13 gives hybrid ILES–RANS vorticity (Frame (a)) and turbulence

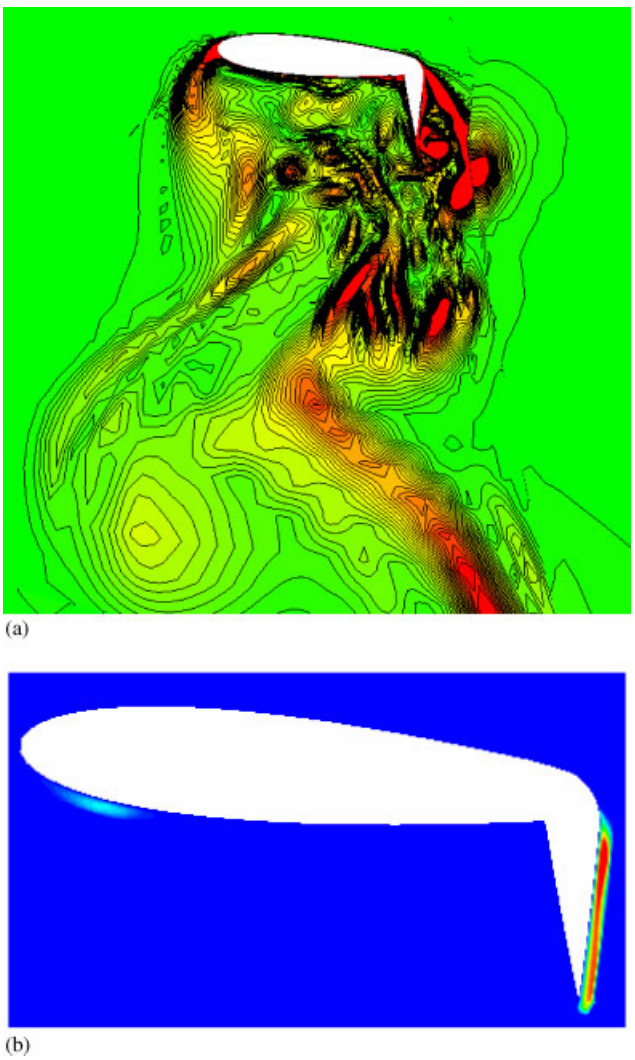

Figure 13. Hybrid ILES–RANS vorticity and turbulence viscosity contours for generic tilt-rotor wing geometry: (a) vorticity contours; and (b) viscosity contours.

viscosity contours (Frame (b)). In Frame (a) large coherent vortex structures can be observed. The Strouhal number for these is about 0.2 (based on the wing chord), this being a plausible bluff body value. As can be seen from Frame (b) the lack of boundary layer shear and the oncoming flow with no modelled eddy viscosity results in only a small fraction of boundary layer RANS modelling, this occurring on the right-hand side flap surface. Without this small RANS zone, the solution would be pure ILES. However, incorporation of the small RANS component increases the predicted drag by over 14% !!. Hence the importance of the boundary layer modelling and the dangers of using pure ILES is clear.

4. CONCLUSIONS

Simulations have been made for high angle of attack NACA0012, wing–flap, generic tilt-rotor airfoil and double-delta geometry flows. These are all problem flows for URANS models. The following URANS models were tested: SA; Menter SST and the EASM. Also, SA and Menter SST versions of DES were tried along with the ILES–RANS approach. The latter is intended for flexible geometry high-speed-flow solvers. Understandably, such codes are relatively dissipative. As shown for the DES NACA0012 even fifth-order upwinding is too dissipative. Although not used in all the results, the hybrid ILES–RANS length scales can be generated and controlled using a Hamilton–Jacobi equation. The standard turbulence modelling approaches were found to give perhaps a surprising results variation. Results suggested that the EASM and Menter SST URANS models were more accurate than SA (with no rotation correction). However, the EASM is found very challenging to converge. The hybrid ILES–RANS results are generally considerably better than pure ILES. They also give sensible lift and drag values for flows with low levels of separation. Such flows are especially challenging for hybrid RANS-eddy resolving approaches.

APPENDIX A

A.1. Plane channel flow validation case

These $Re_\tau \approx 1000$ simulations use $\alpha = 0$, $N_{CD} = 2$ and the temporal discretization acts to dissipate turbulence. The grid and domain size is such that at first off-wall nodes $y^+ \approx 1$ with

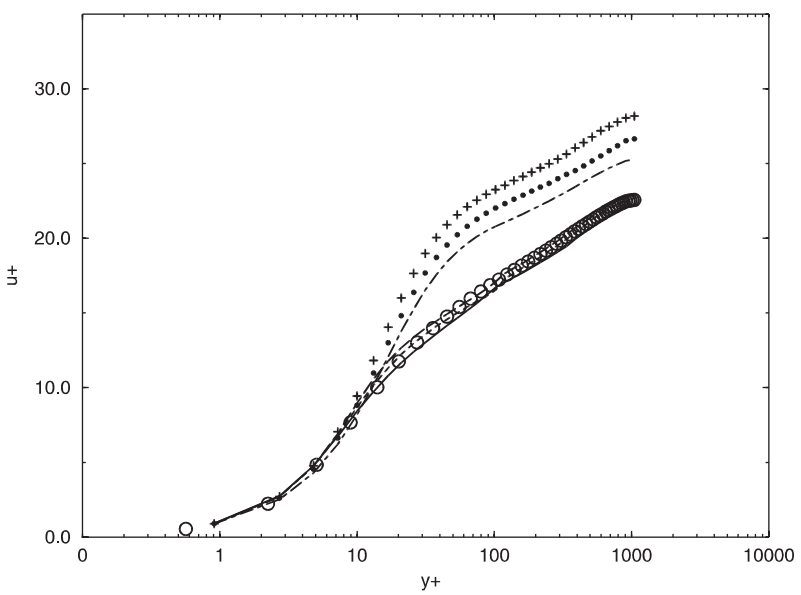

Figure A1. Plane channel flow 'law of the wall.' (◯, 'benchmark' data; ____ $\varepsilon_0 = 0.2$, $\varepsilon_1 = 0$; _ _ _ _ $\varepsilon_0 = 0.2$, $\varepsilon_1 = 1.5$ and $m = 1$; - - - - - $\varepsilon_0 = \varepsilon_1 = 0$; _ · _ · _ · _ · _ non-linear LES; +, ILES; .... LES).

$\Delta x^+ \approx 200$ and $\Delta z^+ \approx 100$. Hence, the latter spacing is inadequate for LES near wall streak resolution. Figure A1 gives fully developed flow law of the walls. The O symbols represent benchmark LES data [31]. Incidentally, this LES data is in virtually perfect agreement with the measurements of Reference [32]. Non-linear Kosovic [33] and linear Yoshizawa [34] k–l subgrid scale based LES results are given by the chain-dashed and dotted lines, respectively. More details on the Kosovic modelling can be found in Reference [22]. The + symbols give the pure ILES solution. As can be seen, and expected, the pure ILES and linear LES wall laws are poor. The non-linear LES model improves agreement. Hybrid ILES–RANS results for the Figure 2 $\tilde{d}$ scales are also shown in Figure A1. To help identify them, they keep Figure 2 line styles. As can be seen, inclusion of near wall RANS modelling, with the lower dissipation ILES away from walls, has produced a greatly improved law of the wall. For all ε_0, ε_1 values resolved turbulence stress components are very similar to the k–l based hybrid RANS-LES results in Reference [7], this code being used for these channel flow simulations.

ACKNOWLEDGEMENTS

Cases (c) and (d) were primarily carried out at Boeing Commercial Airplanes, Seattle with enhancements to the distance function computations being made at a subsequent NASA Langley visit. Especial thanks are due to P. R. Spalart for making the former visit possible and for his very generous encouragement and support during it. Especial thanks are also due to C. Hilmes. Also I would like to thank the NTS group for allowing the use of their excellent and pleasant to use code. Dr L. Hedges kindly generated the Case (b) grid and Dr M. Hong provided the Case (c) set-up with mesh. I am grateful for this help. Funding by the U.K. Royal Academy of Engineering and Boeing are gratefully acknowledged.

REFERENCES

1. Spalart PR, Allmaras SR. A one-equation turbulence model for aerodynamic flows. *La Recherche Aerospatiale* 1994; **1**:5–21.
2. Wilcox DC. Turbulence modelling for CFD, DCW Industries, 1998.
3. Menter FR. Zonal two equation k–ω turbulence models for aerodynamic flows. *AIAA Paper AIAA-93-2906*, 1993.
4. Davidson L. Prediction of the flow around an airfoil using a Reynolds stress model. *ASME Journal of Fluids Engineering* 1995; **117**:50–57.
5. Gatski TB, Speziale CG. On explicit algebraic stress models for complex turbulent flows. *Journal of Fluid Mechanics* 1993; **254**:59–78.
6. Shur M, Spalart PR, Strelets M, Travin A. Detached-eddy simulation of an aerofoil at high angle of attack. *Proceedings of the Fourth International Symposium on Engineering Turbulence Modelling and Measurements*, Ajaccio, Corsica, France, 1999; 669–678.
7. Tucker PG, Davidson L. Zonal k–l based large eddy simulations. *Computers and Fluids* 2003; **33**:267–287.
8. Davidson L, Dahlstrom S. Hybrid LES–RANS: an approach to making LES applicable at high Reynolds number. In *Proceedings of CHT-04*, *Advances in Computational Heat Transfer III*, de Vahl Davis G, Leonardi E (eds). *Paper Number CHT-04-103* (ISBN: 1-5670-174-2), 2004.
9. Rollet-Miet P, Luarence D, Ferziger J. LES and RANS of turbulent flow in tube bundles. *International Journal of Heat and Fluid Flow* 1999; **20**:241–254.
10. Squires KD, Forsythe JR, Morton SA, Strang WZ, Wurtzler KE, Tomaro RF, Grismer MJ, Spalart PR. Progress on detached-eddy simulation of massively separated flows. *AIAA Paper AIAA-2002-1021*, 2002.
11. Forsythe JR, Hoffmann KA, Squires KD. Detached-eddy simulation with compressibility corrections applied to a supersonic axisymmetric base flow. *AIAA Paper AIAA-2002-0586*, 2002.
12. Mary I, Sagaut P. Large eddy simulation of flow around an airfoil near stall. *AIAA Journal* 2002; **40**(6):1139–1145.
13. Spyropoulos ET, Blaisdell GA. Large-eddy simulation of a spatially evolving supersonic turbulent boundary layer flow. *AIAA Journal* 1998; **36**(11):1983–1990.
14. Kravchenko AG, Moin P. On the effect of numerical errors in large-eddy simulations of turbulent flows. *Journal of Computational Physics* 1997; **131**:310–322.

15. Garnier E, Mossi M, Saguat P, Comte P, Deville M. On the use of shock-capturing schemes for large-eddy simulation. *Journal of Computational Physics* 1999; **153**:273–311.
16. Roe PL. Approximate Riemann solvers, parameter vectors and difference schemes. *Journal of Computational Physics* 1981; **46**:357–378.
17. Dahlstrom S, Davidson L. Large eddy simulation of the flow around an airfoil. *AIAA Paper AIAA 2001-0425*, 2001.
18. Strelets M. Detached eddy simulation of massively separated flows. *AIAA Paper 2001-0879*, 2001.
19. Boris JP, Grinstein FF, Oran ES, Kolbe RL. New insights into large eddy simulation. *Fluid Dynamics Research* 1992; **10**:199–228.
20. Fureby C, Grinstein F. Towards large eddy simulation of flows in complex geometries. *AIAA Paper 98-2806*, 1998.
21. Tucker PG. Novel MILES computations for jet flows and noise. *International Journal of Heat and Fluid Flow* 2004; **25**(4):625–635.
22. Tucker PG. Hybrid MILES–RANS method for more dissipative solvers and the use of non-linear LES, *AIAA Paper AIAA-2004-0071*, 2004.
23. Sethian JA. Fast marching methods. *SIAM Review* 1999; **41**(2):199–235.
24. Wigton LB. Optimizing CFD codes and algorithms for use on Cray computers. *Frontiers of Computational Fluid Dynamics*, Caughey DA, Hafez MM (eds). World Scientific: Singapore, 1998; 1–15 (Chapter 16).
25. Boger DA. Efficient method for calculating wall proximity. *AIAA Journal* 2001; **39**(12):2404–2406.
26. Tucker PG. Differential equation based wall distance computation for DES and RANS. *Journal of Computational Physics* 2003; **190**(1):229–248.
27. Rumsey CL, Lee-Rausch EM, Watson RD. Three-dimensional effects on multi-element high lift computations. *AIAA Paper 2002-0845*, 2002.
28. Temmerman L, Leschziner MA, Hanjalic K. A-priori studies of a near-wall RANS model within a hybrid LES/RANS scheme. *Engineering Turbulence Modelling and Experiments—5*, Rodi W, Fueyo N (eds). Elsevier: Amsterdam, 2002; 317–326.
29. Morton SA, Forsythe JR, Mitchell AM, Hajek D. DES and RANS simulations of delta wing vortical flows. *AIAA paper 2002-0587*, January 2002.
30. Spalart P, Hedges L, Shur M, Travin A. Simulation of active flow control on a stalled airfoil. *Flow, Turbulence and Combustion* 2003; **71**:361–373.
31. Piomelli U. High Reynolds number calculations using the dynamic subgrid-scale stress model. *Physics Fluids* 1993; **5**:1484–1490.
32. Wei T, Willmarth WW. Reynolds-number effects on the structure of a turbulent channel flow. *Journal of Fluid Mechanics* 1989; **204**:57–90.
33. Kosovic B. Subgrid scale modelling for the large eddy simulation of high Reynolds number boundary layers. *Journal of Fluid Mechanics* 1997; **336**:151–182.
34. Yoshizawa A. Bridging between eddy-viscosity-type and second order models using a two-scale DIA. *Ninth International Symposium On Turbulent Shear Flow*, Kyoto, vol. 3, 1993; 23.1.1–23.1.6.

